PAPER

Synergistic chemotherapy and phototherapy co-delivery nanoparticle preparation and anti-triple negative breast cancer study

Fan Yang,[†][a] Hongchi Liu,[†][a] Qian Luo, [iD][b] Hao Deng,[a] Rongrong Zhang,[a] Yi Yang,[a] Hong Yang,[b] Huaying Wu*[a] and Xiaojun Tao [iD] *[a]

In this study, the amphiphilic polymer HA–ANI, formed by grafting hyaluronic acid (HA) and 6-(2-nitroimidazolyl)hexylamine (ANI), was self-assembled in water to form nanoparticles (NPs), which were modified to obtain dual drug-loaded nanoparticles (P/I NPs) by dialysis loading of paclitaxel (PTX) and IR780. Electron microscopy and dynamic light scattering (DLS) results showed that the P/I NPs presented a near-spherical shape with a size of 221.10 ± 2.31 nm. The drug loading and encapsulation rates of PTX in P/I NPs were 22.73% and 89.23%, respectively, and those of IR780 were 1.11% and 42.44%, respectively. In vitro release experiments demonstrated that NADPH could accelerate the drug release from the NPs. Under the irradiation of an NIR laser, the temperature of the P/I NPs increased significantly. In an in vitro cellular assay treating 4T1 cells for 24 h, the cellular uptake rate of NPs could reach 91.50 ± 3.51%, the 4T1 cell migration rate was 2.68 ± 0.34%, the cell viability was 39.96 ± 0.55%, and the apoptotic cell death rate was 13.93 ± 0.42%. In an in vivo anti-tumor experiment, the inhibition rate of the P/I NPs towards tumors was up to 35.44%; the fluorescence intensity at the tumor site gradually increased with time, and the maximum value appeared within 24 h, indicating that the P/I NPs had a targeting function. The results of H&E staining showed that there was no obvious pathological damage to the main organs of the mice in each group, that means there were no obvious side effects.

1 Introduction

Breast cancer can be classified into various types according to its molecular subtypes,[1] among which triple-negative breast cancer (TNBC) lacks targeted therapeutic approaches due to the low expression of estrogen receptor (ER), progesterone receptor (PR), and human epidermal growth factor receptor 2 (HER-2), and the current therapeutic approach is mainly dominated by single systemic chemotherapy. Moreover, TNBC is highly metastatic and heterogeneous, with poor prognosis and high recurrence rate after treatment, so new therapeutic approaches are urgently needed.[2–4]

Paclitaxel (PTX) is the first-line drug in the treatment of TNBC, and its main mechanism of action is to inhibit the depolymerisation of microtubule proteins and keep microtubules stable, thus inhibiting mitosis and inducing apoptosis in cancer cells.[5,6] However, PTX often fails in clinical application due to the development of drug resistance in patients,[7,8] so

finding new combination therapies is crucial to improve the therapeutic efficacy. IR780 is a lipophilic cationic heptamethylamine fluorescent dye, and by injecting IR780 into the tumour tissue and irradiating it using an NIR laser, the dye can absorb light energy and convert it into heat, thus destroying tumour cells.[9] However, free IR780 was experimentally found to have the disadvantages of high hydrophobicity, poor photostability, poor tolerance, and high in vivo toxicity, which greatly limit its clinical application.[10,11] Therefore, it is necessary to develop a new drug delivery system to achieve the co-delivery of PTX and IR780 to enhance the therapeutic effect for TNBC patients through phototherapy combined with chemotherapy and to reduce the toxic side effects.

Nanotechnology-based drug delivery systems (DDS) have shown great potential in oncology therapy.[12–14] These systems can effectively deliver drugs to the tumour site and improve drug accumulation and deep penetration, achieving more efficient therapeutic effects.[15–17] Firstly, nanomedicine co-delivery systems can load anticancer drugs with different physicochemical properties into a single system, overcoming problems in drug transport mechanisms and biodistribution in vivo.[18] Secondly, by adjusting the size and surface properties of the nanoparticles, the enhanced permeability and retention (EPR) effect can achieve their accumulation in the tumour, and then through active targeting to achieve active recognition and

[a]Key Laboratory of Study and Discovery of Small Targeted Molecules of Hunan Province, School of Medicine, Hunan Normal University, Changsha 410013, China. E-mail: HuayingWu6@hunnu.edu.cn; taoxiaojun1981@outlook.com

[b]Department of Oncology, Hunan Normal University First Affiliated Hospital Hunan Provincial People's Hospital, Changsha 410005, China

† These authors contributed equally to this work.

binding to tumour cells.[19] Finally, the design of pH-sensitive,[20] reactive oxygen species (ROS)-responsive,[21] redox-responsive[22] and light-responsive[23] nano-delivery systems can accurately control the release of drugs inside the tumour cells to achieve efficient drug utilisation and effective treatment. These systems take advantage of the unique microenvironment inside the tumour cells, such as decreased pH, increased ROS levels or changes in redox potential, to trigger the precise release of drugs, to enhance the therapeutic efficacy and reduce the toxicity to normal tissues.[24,25] Amphiphilic polymers are block copolymers consisting of hydrophilic and hydrophobic segments that are highly effective drug delivery platforms in cancer therapy due to their self-assembly (*e.g.* formation of micelles or vesicles), stimulus responsiveness (pH, enzyme or ROS trigger release), and biocompatibility. Advantages include improved solubility of hydrophobic drugs such as paclitaxel, passive targeting using tumor EPR effects, reduction of toxic side effects through slow release, and use as a multifunctional vector in combination with chemotherapy, gene therapy, and immunomodulators. However, the potential toxicity of polymer degradation products, inadequacy of micellar stability (CMC-dependent), production process complexity, and PEG related immunogenicity still need to be addressed. In recent years, research has focused on novel stimulus-responsive materials (such as ROS-sensitive polymers), non-PEG designs (to reduce immunogenicity), bionic delivery systems (cell membrane camouflage), and combinations with immunotherapies (such as co-loaded chemotherapeutics and PD-1 inhibitors) to enhance tumor specificity and efficacy. In the future, combining intelligent design (multi-target response) and advanced preparation technology (microfluidic, AI optimization), amphiphilic polymers are expected to promote the development of personalized medicine for integrated cancer diagnosis and treatment. The self-assembly of amphiphilic polymers refers to the process in which polymer molecules with both hydrophilic and hydrophobic properties spontaneously form ordered structures through intermolecular interactions in aqueous solutions. This mechanism usually relies on non-covalent interactions such as hydrogen bonding, van der Waals forces, π–π stacking, and hydrophobic effects between molecular segments, thereby constructing nanostructures with specific functions at the microscale. The application of hyaluronic acid (HA) in biomedicine, especially in nano-delivery systems, has been widely noticed and investigated. HA provides a powerful support for precise drug delivery and efficient therapy with its unique physicochemical properties and functions.[26,27] HA has good biocompatibility and non-immunogenicity as a natural polysaccharide, which makes it able to reduce the immunogenic response to the body and decrease side effects.[28,29] The surface of the HA molecule is rich in several easily modifiable functional groups, such as carboxyl groups, which facilitates the loading and controlled release of drugs.[30] In addition, HA is highly expressed in colon, breast, ovarian and other cancer cells, whereas its expression is highly conserved in normal tissues.[31,32] HA enters cells through specific binding to the cell membrane surface receptor CD44 and through receptor-mediated endocytosis.[33] This active targeting strategy allows

the drug to reach the diseased tissue more accurately and improves the therapeutic efficacy.

In this study, we designed an HA-modified HA–ANI nanoparticle loaded with PTX and IR780. Its morphology, particle size distribution, short-term storage stability and *in vitro* release properties were characterised. At the *in vitro* cell level, 4T1 cells were selected for *in vitro* cell uptake studies, cytotoxicity assays, cell migration, and cell apoptosis induction studies to evaluate the *in vitro* biological properties of the nanoparticles. Finally, we established a nude mouse model of triple-negative breast cancer. The distribution of the nanoparticles *in vivo*, the growth inhibitory effect on tumours and the histological changes in the nude mice were further investigated. The *in vivo* and *in vitro* biological efficacy of the dual drug-loaded nanoparticles was comprehensively evaluated.

2 Materials and methods

2.1 Materials

2-Nitroimidazole and *tert*-butyl (6-bromohexyl)carbamate were purchased from Bidepharm, anhydrous potassium carbonate, *N,N*-dimethylformamide, methanol, ethyl acetate, dimethyl sulfoxide (DMSO) and ethanol were purchased from Sinopharm, 1-ethyl-(3-dimethylaminopropyl)carbodiimide hydrochloride, paclitaxel, 1-NADPH and potassium bromide were purchased from Aladdin, *N*-hydroxysuccinimide and IR780 from Macklin, sodium hyaluronate from BLOOMAGE BIOTECH, high-sugar DMEM medium, phosphate buffered solution (PBS), trypsin (with EDTA), penicillin–streptomycin mixture (100×) and serum-free freezing solution from Gibco, fetal bovine serum (FBS) was purchased from BI, tetramethyl azole salt (MTT), 4′,6-diamidino-2-phenylindole (DAPI), 4% paraformaldehyde, saline and chloral hydrate were purchased from Beyotime, Annexin V–FITC/PI apoptosis detection kit was purchased from Maokang Biotechnology, and 4 week-old Balb/c female nude mice were purchased from Jiangsu Jicui Pharmachem.

2.2 Methods

2.2.1 Synthesis of HA–ANI. 2-Nitroimidazole (150 mg; 1.33 mmol) and K$_2$CO$_3$ (280 mg; 2.03 mmol) were dissolved in dimethylformamide (DMF), and then *tert*-butyl (6-bromohexyl) carbamate (390 mg; 1.39 mmol) was added to the DMF solution and it was stirred at 80 °C for 4 hours; the solid impurities were removed by filtration and washed with methanol, and the solid product was obtained by evaporating the residual solvent. The solid was suspended in deionized water and extracted with ethyl acetate, the organic layer was collected, and the BOC-protected 6-(2-nitroimidazole) hexylamine (QANI) was spun. The product was redissolved in methanol. 5 mL of 1.25 M HCl was added into the methanol solution and it was stirred at room temperature for 24 h. The product ANI is then obtained by removing the solvent from the reaction mixture using a rotary evaporator.

Synthesis of HA–ANI polymer with different feed ratio. 60 mg HA (molecular weight about 30 kDa) was dissolved in water and 1-ethyl-(3 dimethylaminopropyl) carbodiimide hydrochloride

(EDCI·HCl) was added (107.35 mg; 0.56 mmol) and N-hydroxysuccinimide (NHS) (64.40 mg; 0.56 mmol) was added, and stirred at room temperature for 1 h; ANI (30 mg; 0.14 mmol) was added to the mixture and it was reacted at room temperature for 24 h; the reaction mixture was transferred into a dialysis bag (MW = 3000) for dialysis. After the solvent was cleaned and pre-frozen at −20 °C, the product HA–ANI was obtained by freeze-drying. Different proportions of HA–ANI polymers were prepared by adjusting the feed mass ratio of HA and ANI to 1.9 : 1 and 1.8 : 1 respectively in the same operation method as above.

2.2.2 Infrared spectroscopy characterization of polymer HA–ANI. First, small amounts of the dry solids of HA, 2-nitroimidazole, ANI, and HA–ANI are removed separately to ensure that each sample is fully dried and free of impurities. Then, a little of each sample is taken out into the mortar for grinding, and when it is ground to powder, an appropriate amount of potassium bromide powder is added and grinding continued; when it is fully ground into powder, an appropriate amount of powder is put into the tablet mold, and the finely ground mixture is pressed into a sheet by a tablet press. Finally, the prepared slices were put into the infrared spectrometer for infrared spectrum determination. During the determination process, the scanning range is set to 500–4000 cm^{-1} to ensure that all infrared absorption peaks of the sample in this range can be captured. The spectra were derived and the structure of the compound was analyzed.

2.2.3 Characterization of polymer HA–ANI by ^{1}H NMR spectroscopy. About 10 mg of the samples to be measured (HA, 2-nitroimidazole, ANI and HA–ANI) were dissolved in appropriate solvents. HA and HA–ANI were dissolved in deuterated heavy water (H$_2$O-d6), and 2-nitroimidazole and ANI were dissolved in deuterated dimethyl sulfoxide (DMSO-d6). The prepared sample solution was transferred into the NMR tube. After the NMR instrument is opened and relevant parameters are set, the NMR tube containing the sample is carefully placed into the probe of the NMR instrument to ensure good contact between the NMR tube and the probe. The M.R.I. was activated and the scanning started. After the scanning was completed, the instrument automatically processed the collected data to generate the ^{1}H NMR spectrum. Based on the position, intensity and shape of the peaks in the spectra, the types and quantities of hydrogen atoms in the compounds HA, 2-nitroimidazole, ANI and HA–ANI in this experiment and their interactions were deduced.

2.2.4 Preparation of P/I NPs and HA–ANI NPs. About 10 mg of HA–ANI polymer was dissolved in DMSO and stirred at 40 °C for 2 h. About 5 mg of PTX and 1 mg of IR780 were pre-dissolved in an appropriate amount of DMSO, and then mixed with the HA–ANI solution and stirring was continued at 40 °C for 4 h (Fig. 1). Subsequently, the liquid mixtures were transferred to dialysis bags (MW = 3000) and dialyzed with deionized water to remove the DMSO completely. P/I NPs were obtained by freeze-drying in a freeze-dryer after pre-freezing at −20 °C. Blank nanoparticles HA–ANI NPs were prepared in the same way.

2.2.5 Determination of particle size, zeta potential and PDI of P/I NPs and HA–ANI NPs. 1 mg of P/I NPs prepared above was dissolved in 1 mL of purified water to form a 1 mg mL^{-1} solution of P/I NPs, which was then transferred to the cuvette of the DLS to determine the size of P/I NPs, the zeta potential and the polydispersity index (PDI). The size, zeta potential and PDI of ANI NPs were determined in the same way.

2.2.6 Morphological observation of P/I NPs and HA–ANI NPs. The prepared P/I NPs solution was added dropwise onto a copper mesh and the sample was allowed to dry naturally at room temperature. The prepared copper mesh was placed into the sample chamber of the transmission electron microscope. The parameters of the electron microscope, such as accelerating voltage, electron beam intensity and magnification, were adjusted to obtain a clear image. The morphology, size and dispersion of P/I NPs and HA–ANI NPs were observed and recorded.

2.2.7 Stability of P/I NPs. The P/I NPs were stored at room temperature, and the particle size, zeta potential and PDI were measured by dynamic light scattering on the 1st, 3rd, 5th and 7th days, and the changes in the relevant parameters were observed during the 7 days.

2.2.8 Determination of drug loading and encapsulation rate. 5 mg of paclitaxel and IR780 were dissolved in 25 mL of DMSO to form a 200 μg mL^{-1} standard stock solution, and then diluted into a series of 0.5 μg mL^{-1}, 1 μg mL^{-1}, 5 μg mL^{-1}, 10 μg mL^{-1}, 15 μg mL^{-1}, 20 μg mL^{-1}, 30 μg mL^{-1}, and 40 μg mL^{-1} solutions by the dilution method. 40 μg mL^{-1} was used to plot the standard curve of paclitaxel. At the same time, the IR780 standard stock solution was diluted to 1 μg mL^{-1}, 2 μg mL^{-1}, 4 μg mL^{-1}, 6 μg mL^{-1}, 8 μg mL^{-1} and 10 μg mL^{-1} by the dilution method, and then the standard curve of IR780 was plotted. The absorbance of 3 mL of the P/I NPs solution was measured by UV spectrophotometry, and the loading capacity and encapsulation rate of PTX and IR780 in P/I NPs were calculated by the standard curve equation.

$$\text{Drug loading capacity [LC (\%)]} = \frac{W_{\text{loaded}}}{W_{\text{P/I NPs}}} \times 100\% \quad (1)$$

$$\text{Encapsulation efficiency [EE (\%)]} = \frac{W_{\text{loaded}}}{W_{\text{added}}} \times 100\% \quad (2)$$

where W_{loaded} is the weight of drug successfully loaded, $W_{\text{P/I NPs}}$ is the total weight of the nanoparticles, and W_{added} is the total weight of drug initially added.

2.2.9 *In vitro* release of PTX from P/I NPs. 1 mL volumes of 1 mg mL^{-1} P/I NPs and 1 mg mL^{-1} P/I NPs containing 10 mM NADPH, 100 μM NADPH, and 10 μM NADPH were accurately measured and each put into a dialysis bag (MW = 3000), which was then placed into 150 mL of PBS buffer at pH 7.4, and shaken at 37 °C and 100 rpm, protected from light. 3 mL of the release medium was taken at the time points of 0, 0.5, 1, 2, 4, 8, 12, 24, 36, 48, 60, and 72 h, and 3 mL of blank medium was added, and the absorbance of PTX at 229 nm was measured by UV spectrophotometry, and the cumulative release rate was calculated according to the following formula.

$$Q \ (\%) = \left(C_n \times V + V_n \times \sum_{t=0}^{n} C_i \right) \Big/ W_{\text{loaded}} \times 100\% \quad (3)$$
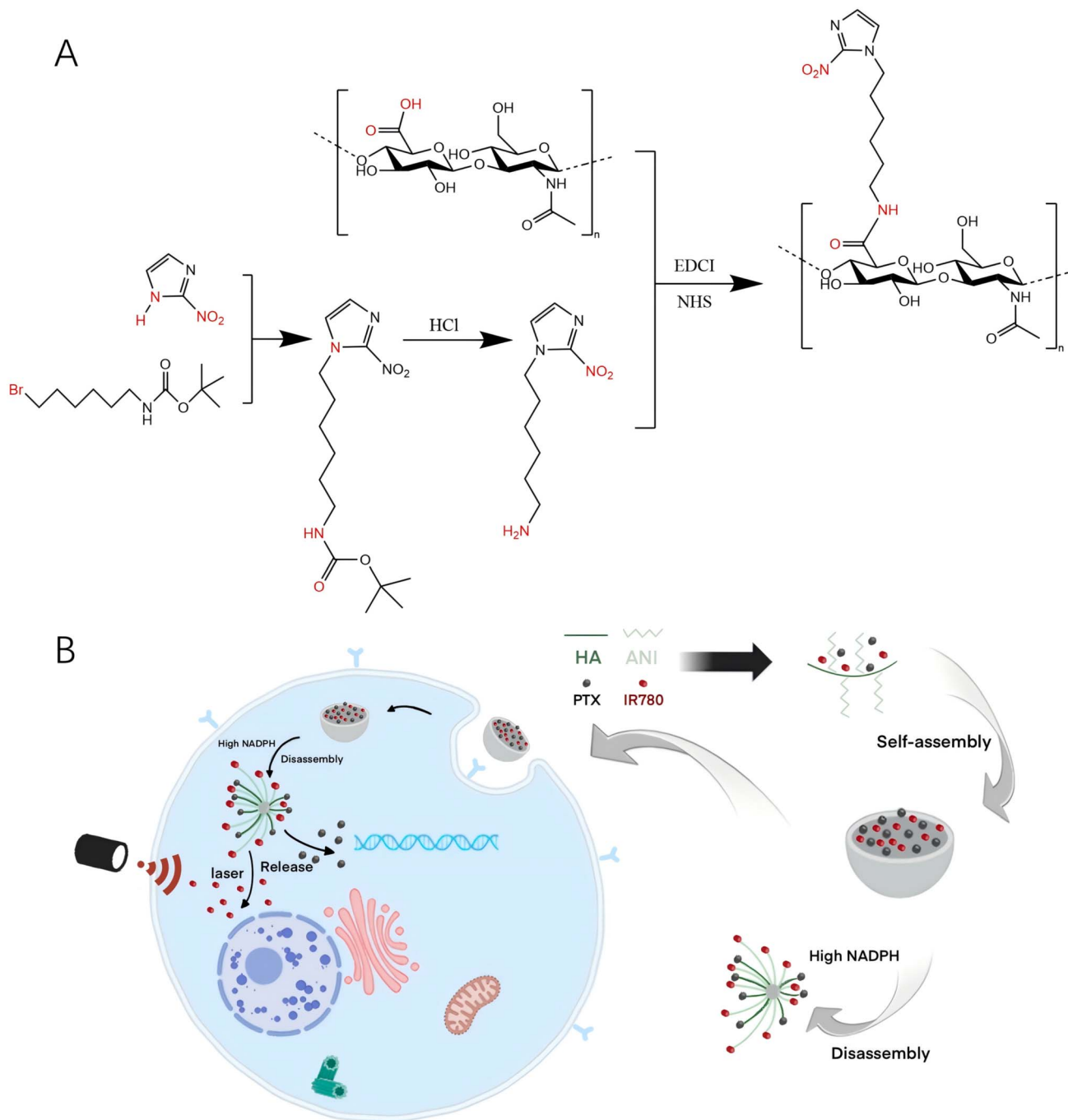
Fig. 1 (A) Synthesis of HA–ANI. (B) Schematic representation of the preparation of P/I NPs and a schematic diagram of the combination therapy.

where W_{loaded} is the weight of the drug contained in the nanoparticles, C_n is the concentration of the sample at T_n, V is the total volume of the release medium, V_n is the volume of the sample and C_i is the concentration of the sample at T_i. ($i = 0$, 0.5, 1, …, 72 h; V_0, C_0 equal to 0).

2.2.10 *In vitro* photothermal effect assay for P/I NPs. In order to study the photothermal conversion efficiency of P/I NPs, PBS, free PTX, PTX NPs, free IR780, free P/I, and P/I NPs ($C_{IR780} = 5$ μg mL^{-1}) were irradiated with a near-infrared laser (808 nm, 2 W cm^{-2}) for 3 min The laser-induced temperature

changes as well as the thermal images of different drug solutions were recorded by a hand-held thermal imaging camera at 30 s intervals. In addition, the temperature changes of different concentrations of P/I NPs ($C_{IR780} = 1$, 5, 10 and 15 μg mL^{-1}) under laser irradiation were also recorded. In order to further investigate the effect of repeated laser irradiation on the photothermal efficiency of the drugs, the free IR780 and P/I NPs ($C_{IR780} = 5$ μg mL^{-1}) were irradiated with the 808 nm near-infrared laser for 3 min and then allowed to cool down naturally to room temperature, and the heating–cooling process was

repeated three times, and the changes in temperature were recorded by using hand-held thermostatic thermal imaging.

2.2.11 Cell uptake. 4T1 cells in logarithmic growth phase were seeded in 6-well plates (2 mL, 5×10^4 cells per well) and incubated at 37 °C, 5% CO_2 incubator, for 24 h until the cell attachment and fusion rate reached 80%, then the old culture medium was discarded from the wells, and a new culture medium containing free P/I and P/I NPs was added, in which $C_{IR780} = 1$ μg mL^{-1}. Each well was irradiated with the near infrared laser (808 nm; 2 W cm^{-2}) for 3 min, then incubated in a cell culture incubator for 24 h, then the culture medium was aspirated and discarded, and the cells were washed gently with PBS three times, and then the cells were fixed by adding 1 mL of 4% paraformaldehyde to each well for 15 min at room temperature, and then stained with DAPI stain for 5 min, and then the images were captured under an inverted fluorescence microscope.

2.2.12 Cell migration. Cell migration was studied by scratch assay. A 6-well plate was taken and a horizontal line was drawn on the bottom of the plate with a marker in advance. Then, 4T1 cells in logarithmic growth phase were seeded in the 6-well plate (2 mL, 1×10^5 cells per well) and cultured at 37 °C with 5% CO_2 for 24 hours until the cell wall fusion rate reached 100%. A straight line was drawn perpendicular to the bottom of the plate with a 10 μL tip in the wells, and the scratched cells were washed slowly with PBS, followed by the addition of serum-free DMEM containing PBS, PTX, PTX NPs, IR780, P/I, and P/I NPs, in which $C_{PTX} = 0.5$ μM; $C_{IR780} = 0.028$ μM, and each well was irradiated with a NIR laser (808 nm; 2 W cm^{-2}) for 3 min, and then returned to the incubator for continued culture. The migration images were taken at four time points, 0, 6, 12 and 24 hours after dosing.

2.2.13 Cell viability. The cytotoxicity study was performed using the MTT method. 4T1 cells in logarithmic growth phase were seeded in 96-well plates (100 μL, 5000 cells per well) and cultured at 37 °C in a 5% CO_2 incubator for 24 h until the cells were completely adhered to the wall. The cells were treated with a series of PTX, PTX NPs, IR780, P/I and P/I NPs at concentrations of $C_{PTX} = 0.25$ μM, 0.5 μM, 1 μM, 2 μM, and 4 μM; and $C_{IR780} = 0.014$ μM, 0.028 μM, 0.056 μM, 0.112 μM, and 0.224 μM, and the cells were irradiated for 3 min with a near-infrared laser (NIR) (0.028 μM). The IR780-containing group was irradiated with NIR laser for 3 min (808 nm; 2 W cm^{-2}) and then cultured in a cell culture incubator for 24 h. The control group was further cultured with an equal volume of PBS, and 10 μL of 5 mg mL^{-1} MTT solution was added to each well after 24 h. The cells were placed in the incubator for 4 h. The incubation solution was carefully discarded, and 150 μL of DMSO was added to each well. After shaking for 15 min at room temperature, the OD value of each well was detected at 490 nm by multifunctional enzyme marker to calculate the cell viability.

2.2.14 Apoptosis detection. 4T1 cells in logarithmic growth phase were inoculated into 6-well plates (2 mL, 1×10^5 cells per well) and cultured in an incubator at 37 °C with 5% CO_2. When the cells grew to 80% density, the cells were treated with culture

medium containing PTX, PTX NPs, IR780, P/I and P/I NPs, in which $C_{PTX} = 0.5$ μM, $C_{IR780} = 0.028$ μM, and the control group was added with an equal amount of PBS, and each well was irradiated with a near-infrared laser for 3 min (808 nm; 2 W cm^{-2}), and then incubation was continued for 24 h in the cell culture incubator. The culture medium was removed, and the cells were washed once with PBS to remove residual drug and culture medium, followed by digestion of cells with trypsin, collection of cell suspension, centrifugation at 1000 rpm for 5 min, removal of supernatant, resuspension of cells with an appropriate amount of PBS, and cell counting, and the cell concentration was adjusted to 5×10^5 cells per mL. FITC/PI apoptosis kit instructions were to take 100 μL of cell suspension to the flow tube, add 5 μL of Annexin V–FITC and 5 μL of PI staining solution, mix gently and incubate at room temperature away from light for 15 min. At the end of the incubation, add 400 μL of PBS to each flow tube, mix gently, put the flow tube into the flow cytometer, and set up an appropriate fluorescence channel to detect Annexin V–FITC and PI apoptosis. The fluorescence signals of Annexin V–FITC and PI were detected, the data were collected and the apoptosis was analysed.

2.2.15 Establishment of triple-negative breast cancer nude mouse model. 4 week-old Balb/c female nude mice were purchased and quarantined for one week without any abnormality. 4T1 cells were collected during the logarithmic growth period, and the cell concentration was adjusted to 1×10^6/100 μL by PBS. 100 μL of 4T1 cell suspension was injected subcutaneously into the axillae of the forelimbs of the nude mice, and the tumour growth was observed every day after a brief observation without any abnormality.

2.2.16 *In vivo* antitumour activity. When the tumour volume reached about 100 mm^3, the 4T1 tumor-bearing mice were divided into six groups ($n = 4$) and the mice received further intravenous administration: Group 1: control (saline only); Group 2: free PTX; Group 3: PTX NPs; Group 4: free IR780; Group 5: free P/I; Group 6: P/I NPs. Paclitaxel was administered at a dose of 5.0 mg kg^{-1} and IR780 at a dose of 2.0 mg kg^{-1}, and each group was injected intravenously into the tail vein on days 1, 4, 7, and 10, and in the case of the IR780 group, the tumour site was irradiated with an NIR laser (808 nm, 2 W cm^{-2}) for 3 min 4 h after the administration of the drug. Tumour diameter and mouse weight were recorded every other day throughout the treatment and tumour volume was calculated as shown in the equation below.

$$\text{Tumor size} = \frac{\text{length} \times \text{width} \times \text{width}}{2} \quad (4)$$

2.2.17 *In vivo* fluorescence imaging. To assess the *in vivo* biodistribution of P/I NPs, tumour-bearing mice were randomly divided into 2 groups ($n = 3$). When the tumour volume reached about 100 mm^3, the tumor-bearing mice were injected with free IR780/PTX and P/I NPs at a dose of 2.0 mg kg^{-1} IR780 in the tail vein, and anaesthetized by intraperitoneal injection of about 60 μL of chloral hydrate (300 μl/100 g), and the live fluorescence images of the mice were obtained using a small animal *in vivo*

fluorescence imaging system at different time points (1, 6, 24 h). After 24 h, the mice were sacrificed, and the major organs of heart, liver, spleen, lung, kidney and tumour tissue were removed for *ex vivo* imaging.

2.2.18 Histological analysis. After 4 treatments, mice were sacrificed on day 13 and the major organs were stained with hematoxylin–eosin (H&E) to assess side effects. Tumour tissue
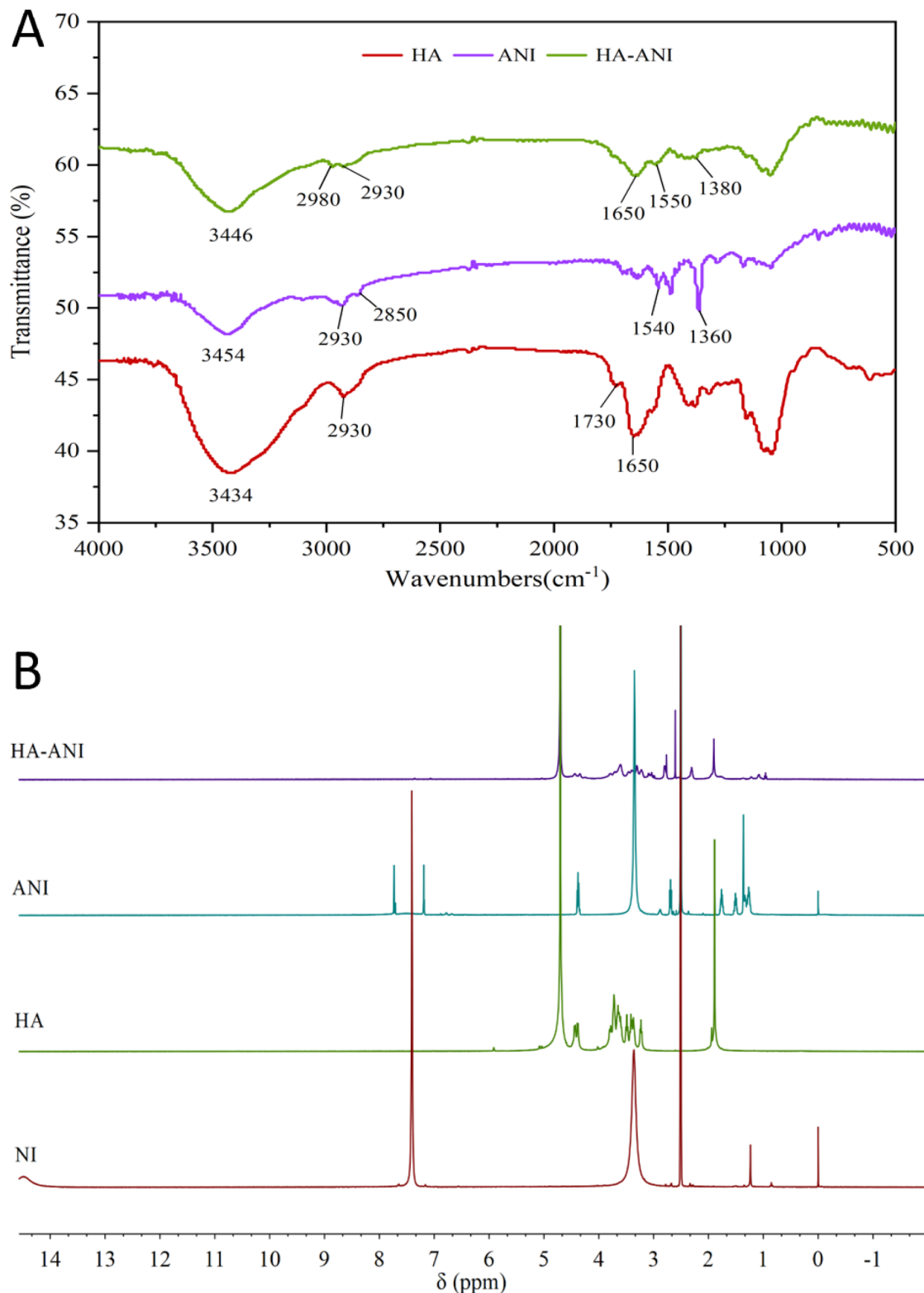
Fig. 2 (A) Infrared spectroscopy characterization of HA, ANI, and polymer HA−ANI. (B) ^{1}H NMR spectroscopy of NI, HA, ANI, and polymer HA−ANI.

sections were stained with H&E, TUNEL and Ki67 to further analyse the *in vivo* anti-tumour effect of P/I NPs.

2.2.19 Statistical analysis. All the experimental results were statistically analysed using GraphPad Prism 9.0, expressed as mean $\pm$ standard deviation ($x \pm s$), and the *t*-test was used to analyse the statistical significance.

3 Results

3.1 Structural characterization of polymer HA–ANI

HA and ANI were grafted using an amide reaction, and the structures of 2-nitroimidazole (NI), HA, ANI and HA–ANI were characterized by infrared spectroscopy and hydrogen NMR (^{1}H-NMR). In the infrared spectrum (Fig. 2A), ANI has a stretching
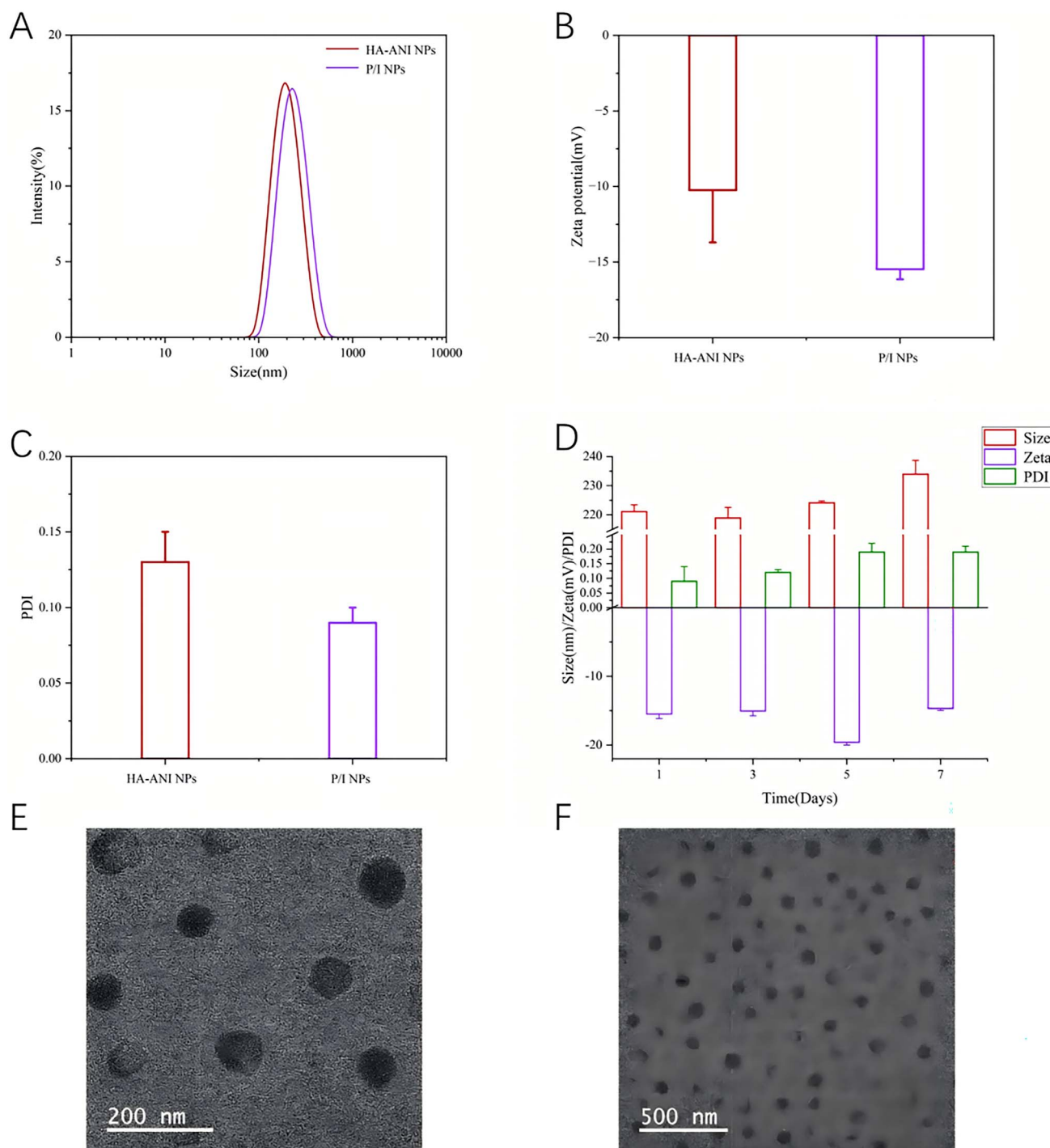
Fig. 3 Characterisation of P/I NP properties. (A) Particle sizes of HA−ANI NPs and P/I NPs. (B) Potentials of HA−ANI NPs and P/I NPs. (C) PDI of HA−ANI NPs and P/I NPs. (D) Stability of P/I NPs stored at room temperature for 7 days. (E) Transmission electron microscopy micrograph of P/I NPs, with a scale bar of 200 nm. (F) Transmission electron microscopy micrograph of P/I NPs, with a scale bar of 500 nm.

vibration absorption for $-NO_2$ at 1360 cm^{-1} and 1540 cm^{-1}, while HA–ANI has a stretching vibration absorption for $-NO_2$ at 1380 cm^{-1} and 1550 cm^{-1}, which moves towards low wavenumber due to conjugation. At the same time, there is the C=O stretching vibration absorption of amide at 1650 cm^{-1}, and the C=O stretching vibration absorption peak of carboxylic acid at 1730 cm^{-1} in HA–ANI disappears. This shows the successful connection of 6-(2-nitroimidazole)hexylamine to hyaluronic acid *via* an amide bond. In the ^{1}H NMR spectrum (Fig. 2B), due to the shielding effect of the heterocyclic rings in HA, the chemical shift of each hydrogen in HA–ANI moves to a higher field. All the results indicated that the synthesis of the HA–ANI polymer was successful.

3.2 P/I NPs preparation and characterisation

Firstly, 2-nitroimidazole was used as the raw material for the preparation of ANI, which was then grafted with HA through acylation to obtain the nanomaterial HA–ANI, and then wrapped with PTX and dialysis of ANI to obtain P/I NPs. Dynamic light scattering showed that the average particle size, zeta potential and PDI of HA–ANI nanoparticles were 186.60 ± 1.28 nm, −10.25 ± 3.45 mV and 0.13 ± 0.02, and for P/I NPs were 221.10 ± 2.31 nm, −15.47 ± 0.67 mV and 0.09 ± 0.05, respectively (Fig. 3A–C). The stability of the nanoparticles was also monitored over a period of 7 days at room temperature, and there was no significant change in any of the three indices (Fig. 3D). Transmission electron microscopy analyses showed (Fig. 3E and F) that the P/I NPs were homogeneous spherical structures with an average size of about 100 nm, which was slightly smaller than that determined by dynamic light scattering (DLS), which was mainly due to the fact that the DLS results were hydrated particle sizes, which were slightly larger than those observed by TEM. The UV-visible spectra were scanned and it was found that PTX had a maximum absorption at 229 nm and IR780 had a maximum absorption at 780 nm (Fig. 4A). The standard curves of PTX and IR780 were plotted at
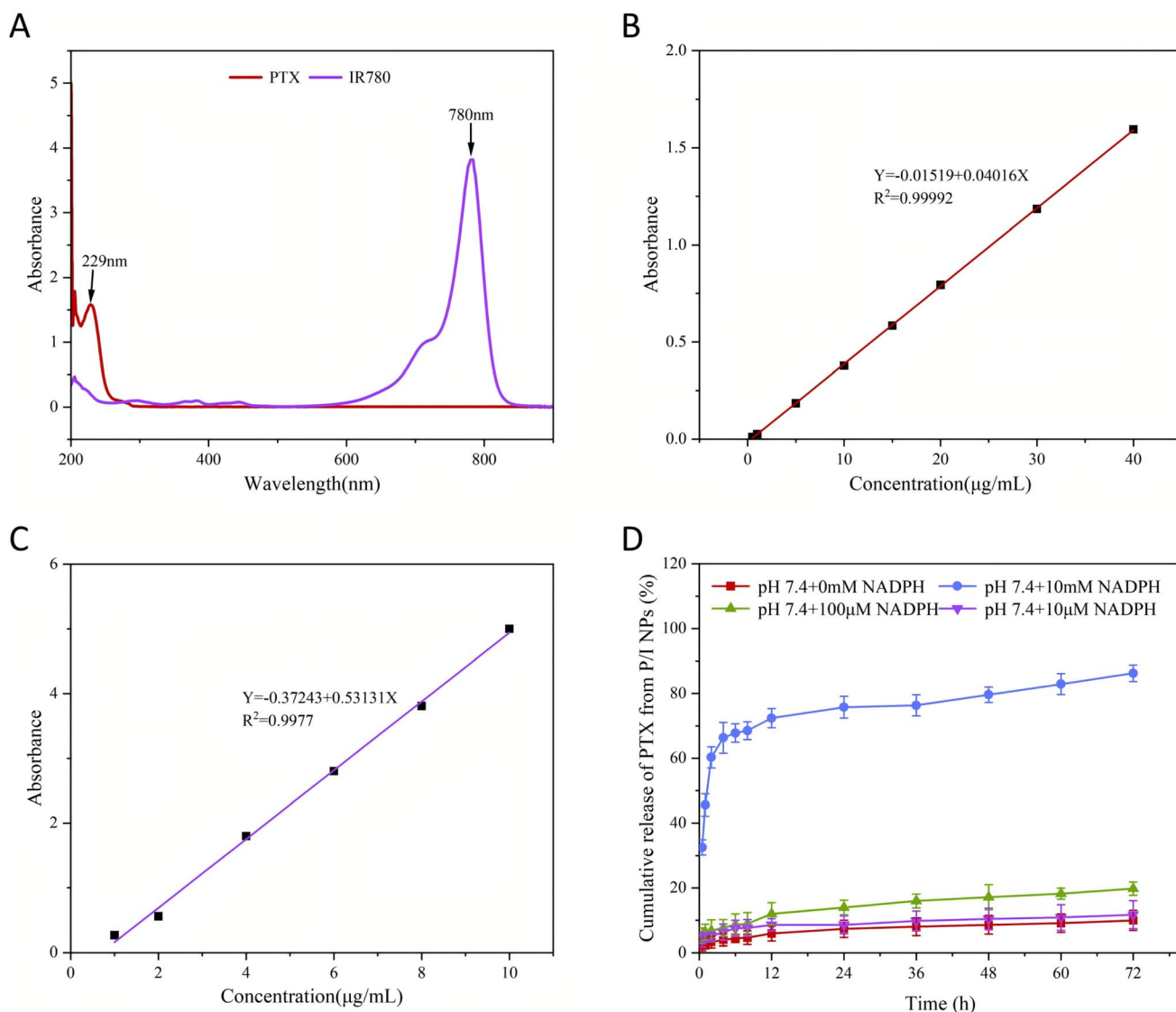

Fig. 4 (A) UV-visible spectra of PTX and IR780. (B) Standard curve of PTX. (C) Standard curve of IR780. (D) Release curve of PTX from P/I NPs.

the two maximum absorption wavelengths (Fig. 4B and C), and then the standard curves were used for the calculation of the loading capacity and encapsulation rate. The loading and encapsulation rates in P/I NPs were 22.73% and 89.23% for PTX and 1.11% and 42.44% for IR780, respectively.

3.3 *In vitro* drug release studies

We further tested the release of PTX from P/I NPs in different environments. About 9.96% of PTX was released in PBS after 72 h, whereas the release rates of PTX in solutions containing 10 mM, 100 μM and 10 μM of NADPH reached 86.24%, 19.78% and 11.70%, respectively (Fig. 4D), which were significantly higher than the cumulative release in PBS. We speculate that this may be due to the high level of NADPH induced reduction of the nitro group to an amino group, which further leads to the

dissociation of nanoparticles for drug release. This selective release model towards reductive tumor microenvironment (TME) would mitigate the side effects of chemotherapy and enable targeted release.

3.4 *In vitro* photothermal efficiency study

In order to evaluate the *in vitro* photothermal efficiency of P/I NPs, the temperature changes of different groups under the irradiation of an 808 nm NIR laser were recorded. Under the irradiation of the NIR laser, the temperature of P/I NPs increased by nearly 25 °C, the temperature of free IR780 increased by nearly 20 °C (Fig. 7 and 6), whereas the temperatures of PBS, PTX, and PTX NPs increased only slightly. IR
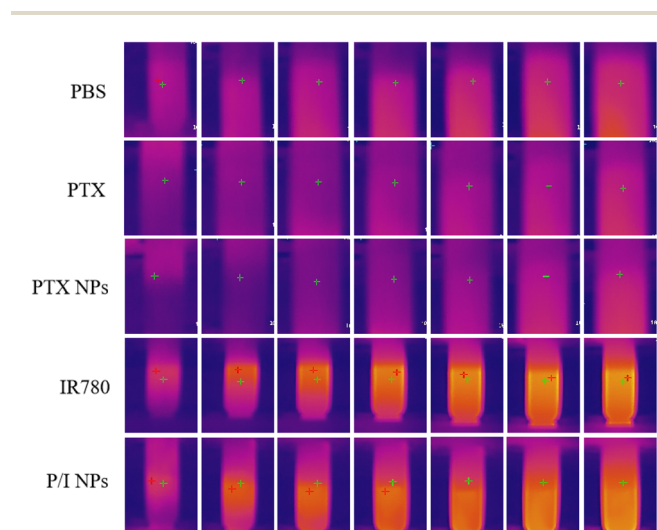

Fig. 5 Infrared thermal images of different formulations irradiated by the NIR laser for 3 min.
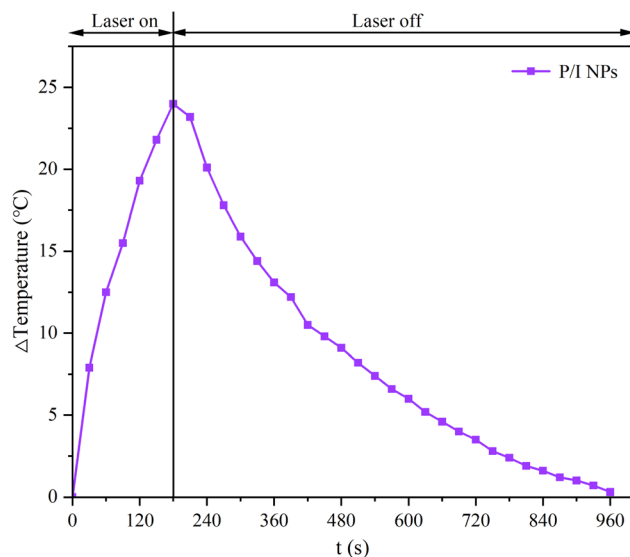

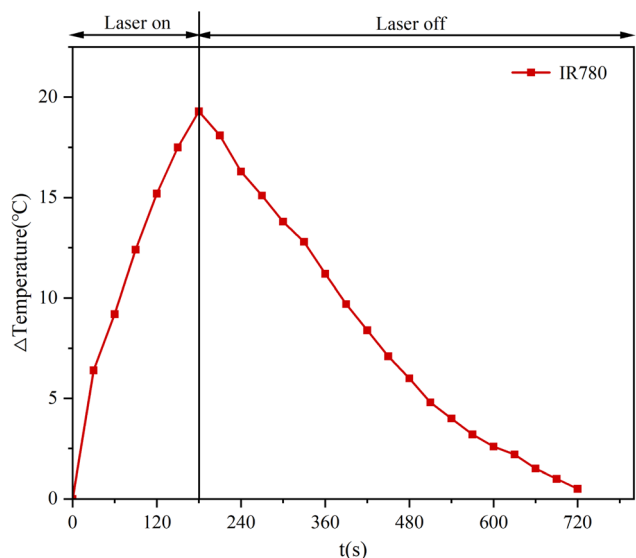Fig. 7 Heating and cooling curves of P/I NPs ($C_{IR780} = 5$ μg mL^{-1}) irradiated by the NIR laser for 3 min.

Fig. 6 Heating and cooling curves of free IR780.

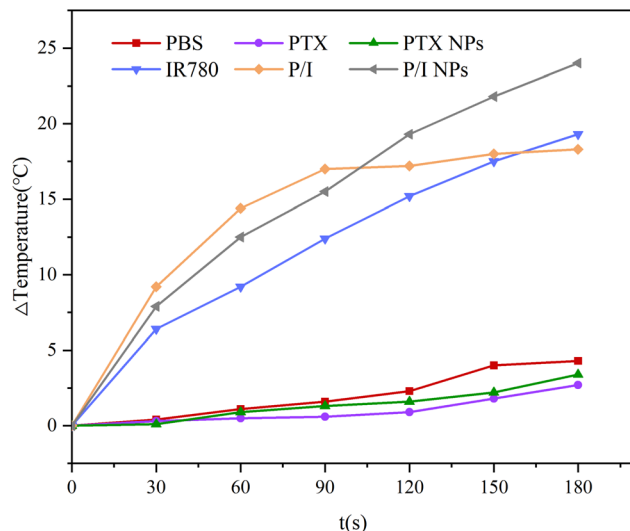

Fig. 8 Temperature changes of different formulations with the same IR780 concentration (5 μg mL^{-1}) during 3 min of NIR laser irradiation.

thermal images visualised the temperature changes in the different drug groups (Fig. 5 and 8). In addition, the temperature changes of P/I NPs under NIR laser irradiation showed a concentration-dependent pattern (Fig. 9), and the temperature increment of P/I NPs under NIR laser irradiation increased from 8 °C to 62.4 °C as the concentration of IR780 increased from 1 μg mL^{-1} to 15 μg mL^{-1}. It has been shown that irreversible cell damage occurs when photothermal therapy produces temperatures above 45 °C.[34] Therefore, loaded IR780 nanoparticles can be used as an effective drug delivery system for photothermal therapy.

To further evaluate the stability of photothermal conversion, we recorded the temperature changes of free IR780 and P/I NPs in three consecutive heating–cooling cycles. After three cycles, the maximum temperature change of the free IR780 decreased

by 5.5 °C, while the maximum temperature change of the P/I NPs decreased by only 2.7 °C (Fig. 10). This was mainly due to the loss of photoactivity due to the photo-induced decomposition of IR780, while the HA–ANI NPs can effectively separate the loaded IR780 from the surrounding environment, thus protecting IR780 from photodegradation and maintaining a stable photothermal conversion capability.

3.5 Cell uptake

We studied the cell uptake and distribution of P/I NPs in a 4T1 mouse breast cancer cell line. The uptake efficiency of P/I NPs by 4T1 cells was observed and analysed using inverted fluorescence microscopy. In addition, P/I NPs-treated 4T1 cells showed significantly enhanced red fluorescence signals at 24 h compared with free IR780, and the cell uptake of P/I NPs in 4T1 cells was significantly decreased when 4T1 cells were pretreated with free HA for 2 h (Fig. 11A), which suggests that the specific binding of HA to the CD44 receptor can significantly promote the internalisation of P/I NPs into the 4T1 cells. Statistical analysis using ImageJ revealed that at 24 h of drug treatment, the cell uptake rate in the P/I NPs-treated group was $91.50 \pm 3.51\%$, which was significantly higher than that in the free P/I group ($16.37 \pm 4.16\%$) and that in the HA-pretreated group ($71.34 \pm 2.65\%$) (Fig. 11B). This was consistent with the results observed by inverted fluorescence microscopy. The above results suggest that P/I NPs can be more effectively endocytosed in tumour cells through specific receptor-mediated endocytosis.

3.6 Apoptosis detection

We used the AnnexinV–FITC/PI Apoptosis Detection Kit to evaluate the apoptosis of different drug treatments. Under NIR laser irradiation, different drugs could induce different degrees of apoptosis after treating 4T1 cells for 24 h (Fig. 11C and D). The apoptosis rate in the P/I NPs group was $13.93 \pm 0.42\%$, which was significantly higher than that in the control group ($0.97 \pm 0.38\%$), the free PTX group ($7.27 \pm 0.59\%$), the PTX NPs group ($3.67 \pm 0.25\%$), the free IR780 group ($2.80 \pm 0.10\%$) and the free P/I group ($8.60 \pm 0.44\%$). We believe that this is mainly due to the enhanced induction of apoptosis caused by the combination of chemotherapy and phototherapy.

3.7 Cell migration

We evaluated the cell migration inhibition effect of different drug treatments using the cell scratch assay. Under near-infrared laser irradiation, the migration inhibition effect of different drugs on 4T1 cells showed time-dependent changes (Fig. 12A and B). When the drugs were treated for 24 h, the cell migration rate in the P/I NPs group was $2.68 \pm 0.34\%$, which was significantly lower than that in the control group ($13.91 \pm 0.80\%$), the PTX group ($7.26 \pm 0.59\%$), the PTX NPs group ($9.76 \pm 0.52\%$), the IR780 group ($8.93 \pm 0.60\%$), and the P/I group ($5.56 \pm 0.43\%$). This indicates that the combination of chemotherapy and phototherapy can significantly inhibit the migration effect of 4T1 cells.
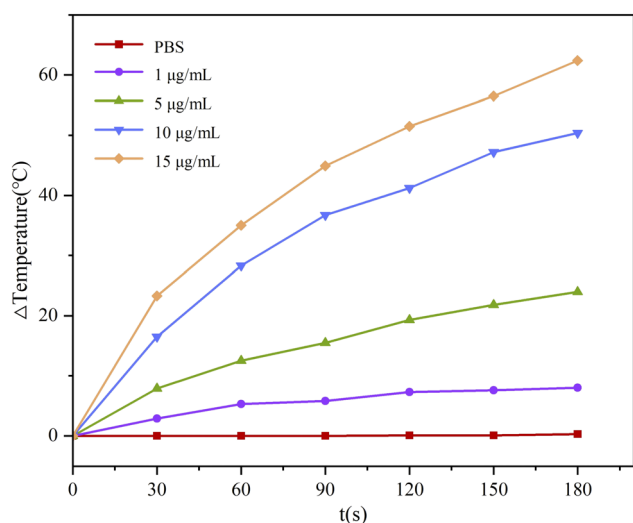

Fig. 9 Temperature changes of different concentrations of P/I NPs during 3 min of NIR laser irradiation.
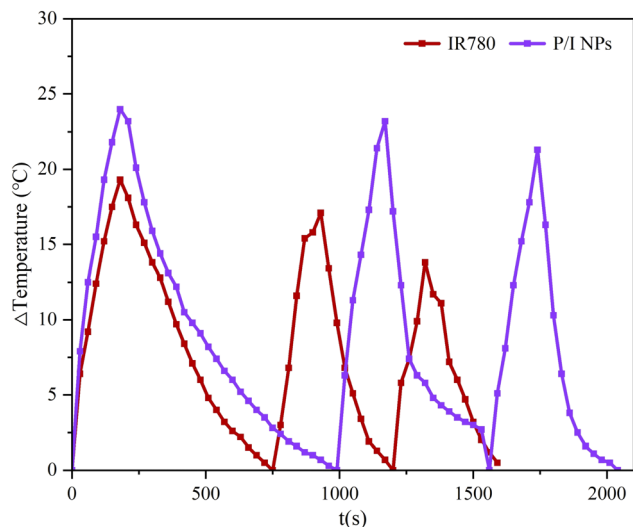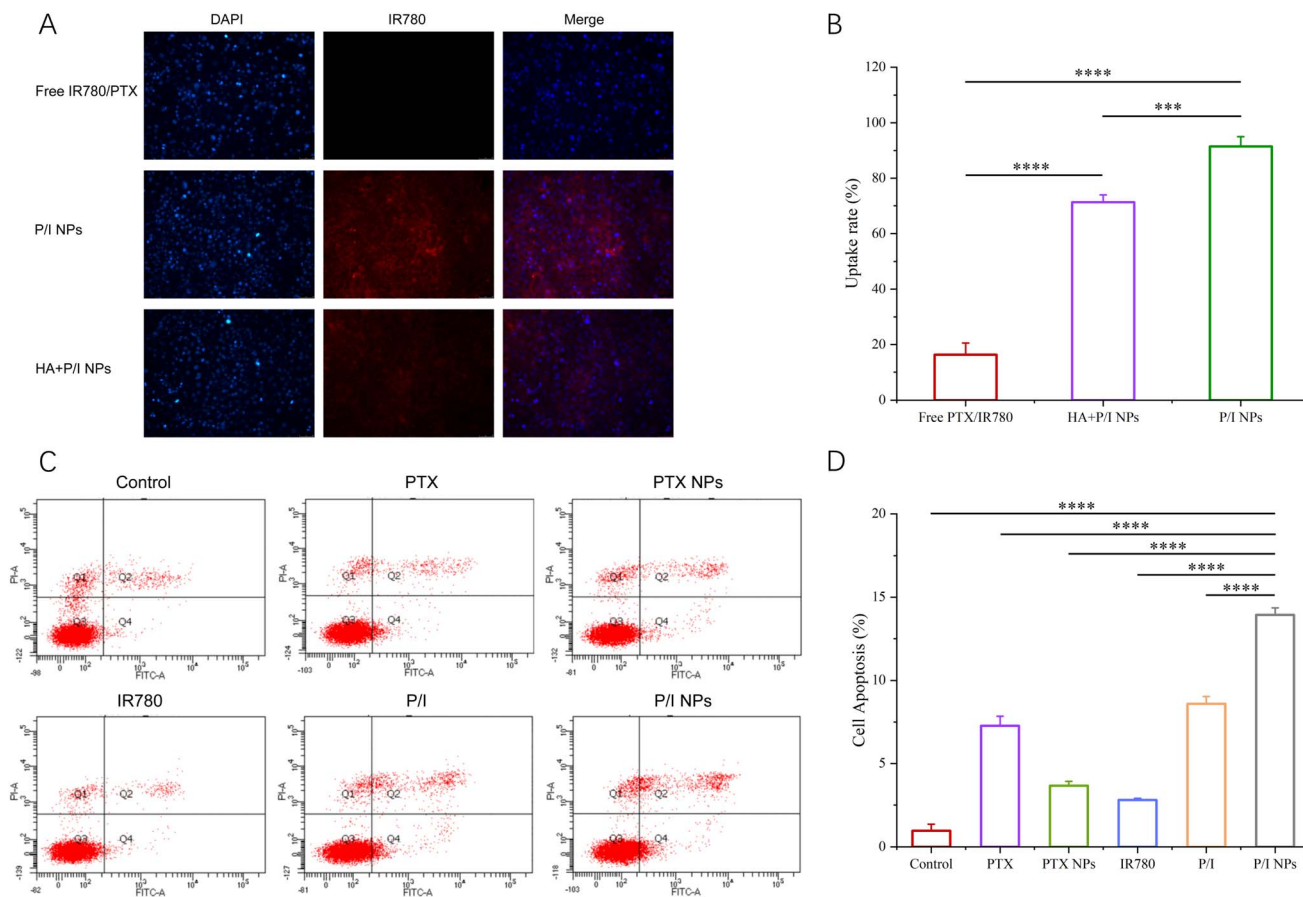

Fig. 10 Temperature changes of free IR780 and P/I NPs ($C_{IR780} = 5$ μg mL^{-1}) during three on/off irradiation cycles.

Fig. 11 Cell uptake studies of 4T1 cells after 24 h of co-incubation with free P/I or P/I NPs and apoptosis of 4T1 cells after treatment with different groups of drugs. (A) Inverted fluorescence microscopy images of 4T1 cells treated with free P/I or P/I NPs; (B) statistical analysis graphs of inverted fluorescence microscopy images using ImageJ software. (C) Flow cytometry determination of apoptosis of 4T1 cells after different treatments; (D) statistical analysis of apoptosis rate. *P < 0.05, **P < 0.01, ***P < 0.001, ****P < 0.0001.

3.8 *In vitro* cytotoxicity

Then we measured the cell viability of 4T1 cells treated with different drugs under NIR laser irradiation using the MTT assay. Under 808 nm NIR laser irradiation, the toxicity of PTX, PTX NPs, IR780, P/I and P/I NPs to 4T1 cells showed concentration-dependent changes, and the 4T1 cells treated with P/I NPs showed a significant reduction in viability at 24 h compared with those treated with control, free PTX, IR780, P/I and PTX NPs (Fig. 12C). The cell viability of 4T1 cells treated with P/I NPs (C_{PTX} = 1 μM, C_{IR780} = 0.056 μM) for 24 h was 39.96 ± 0.55%, which was significantly lower than that of the free PTX group (50.67 ± 2.22%), the PTX NPs group (73.37 ± 4.34%), the free IR780 group (86.23 ± 1.77%), and the free P/I group (56.69 ± 2.31%). We speculate that the enhanced cytotoxic effect of P/I NPs may be due to enhanced cell uptake and the synergistic antitumour effects of chemotherapy and phototherapy.

3.9 *In vivo* anti-tumour therapeutic effect

Based on the significant inhibitory effect of P/I NPs on triple-negative breast cancer 4T1 cells *in vitro*, we further explored its effect on 4T1 tumour-bearing mice. Repeated injections of

different drug treatments were administered on days 1, 4, 7, and 10, respectively. During the 13 day treatment cycle, the P/I NPs-treated group showed better tumour inhibition, with a 59.95% reduction in tumour weight (Fig. 13A), whereas the tumour volume of the saline-treated group increased from 178.93 ± 38.54 mm³ to 908.64 ± 348.63 mm³ (Fig. 13B). Compared with the saline-treated group, the tumour growth of the other treated mice was inhibited to a certain extent, and the tumour growth inhibition (TGI) ratios of the free PTX, PTX NPs, free IR780, and free P/I groups were 30.41%, 17.20%, 26.20%, and 20.34%, respectively, whereas the strongest inhibitory effect was observed in the P/I NPs group, with a TGI of 35.44%, which was mainly due to the fact that the tumours of the P/I NPs group were inhibited to a certain extent due to the synergistic effect of chemotherapy and phototherapy. In addition, the TGI of the P/I NPs group was significantly higher than that of free P/I, which was mainly due to the prolonged blood circulation time of P/I NPs and the increased concentration of tumour accumulation.

3.10 *In vivo* fluorescence imaging

The biodistribution of free P/I and P/I NPs in 4T1 tumour-bearing mice was analysed using a small animal *in vivo*
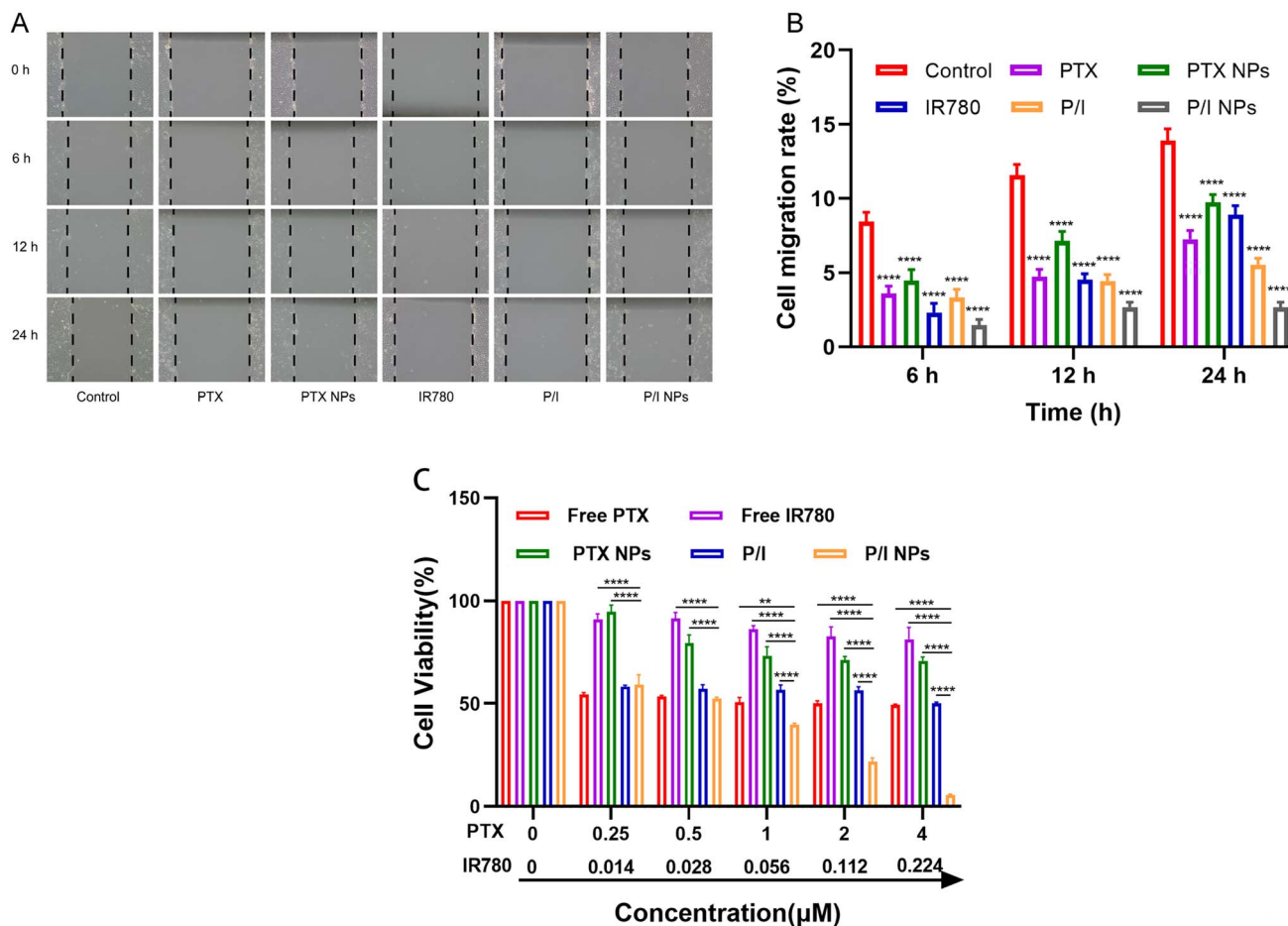
Fig. 12 (A) Migration of different groups of drug-treated 4T1 cells at 0, 6, 12 and 24 h; images taken using a light microscope; (B) statistical analysis of cell mobility; (C) cell viability study of different groups of drug-treated 4T1 cells for 24 h under NIR laser irradiation conditions.

fluorescence imaging system. The fluorescence intensity at the tumour site in the P/I NPs group gradually increased with time, showing the strongest value at 24 h (Fig. 13C), which indicated that P/I NPs could significantly accumulate at the tumour site. In contrast, the weaker fluorescence at the tumour site in the free P/I group was attributed to the fact that the favourable drugs were quickly metabolised by the kidneys after entering the body. After 24 h, the mice were sacrificed and dissected to take out the tumour tissue and major organs, and the fluorescence of the P/I NPs group was found to be significantly stronger than that of the free P/I group (Fig. 13D). In conclusion, P/I NPs have the characteristics of deep tumour penetration, long retention time and favourable fluorescence imaging, and can be used for fluorescence imaging-guided tumour therapy.

3.11 Histological analysis

In order to further observe the systemic toxicity of P/I NPs, a safety evaluation was performed. The results of H&E staining showed that no obvious pathological damage was observed in the main organs of the mice in each group (Fig. 14A). In

addition, to further verify the therapeutic effect, tumour tissues were excised for H&E, TUNEL and Ki67 staining (Fig. 14B). H&E staining showed that the tumour tissue cells increased in the saline-treated group, and the tumour cells in the P/I NPs group were obviously necrotic. Meanwhile, Ki67 staining showed that the cells in the P/I NPs group were less proliferative. In addition, TUNEL staining showed that P/I NPs might induce more apoptosis/necrosis of tumour cells.

4 Discussion

This study developed a novel nanodelivery system, HA–ANI nanoparticles (HA–ANI NPs), for the targeted delivery of paclitaxel (PTX) and IR780 to triple-negative breast cancer cells. The use of hyaluronic acid (HA) to target tumor cells *via* the CD44 receptor has been widely recognized and proven effective. Additionally, the nanoparticle size was designed to be between 200 and 800 nm, allowing them to leverage the enhanced permeability and retention (EPR) effect in tumor tissues to achieve passive targeting and improve drug accumulation at the tumor site. This is also an important strategy in the field of nanoparticle drug delivery. The study also
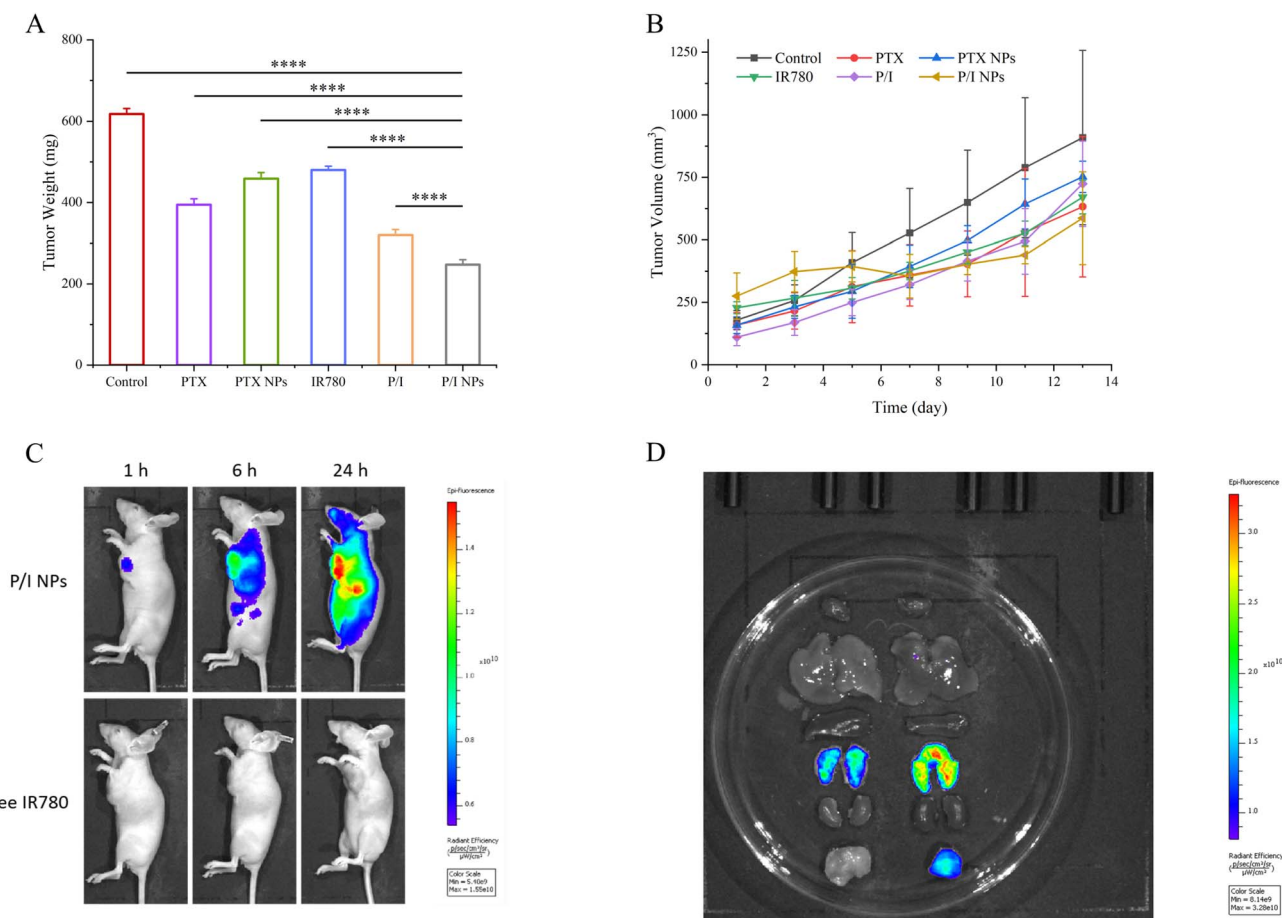
Fig. 13 Mouse tumour weight and volume were monitored on alternate days during the 13 day treatment cycle and biodistribution of free P/I and P/I NPs within 4T1 loaded mice analysed using a small animal *in vivo* fluorescence imaging system. (A) Average tumour weights after different drug treatments; (B) tumour volume change curves after different drug treatments. (C) Distribution of free P/I and P/I NPs in 4T1 tumour–bearing mice at 1 h, 6 h, and 24 h; (D) distribution of free P/I (left) and P/I NPs (right) in heart, liver, spleen, lung, kidney, and tumour tissues of the major organs in mice at 24 h. *$P < 0.05$, **$P < 0.01$, ***$P < 0.001$, ****$P < 0.0001$.

explored the incorporation of 2-nitroimidazole into HA–ANI NPs to investigate its potential for controlled drug release in tumor cells, a concept that has also attracted attention in related research. The experimental results showed that P/I nanoparticles (P/I NPs) had a near-spherical shape, which is conducive to passive targeting through the EPR effect and is consistent with current research consensus. The P/I NPs exhibited high encapsulation efficiency for PTX and IR780 and demonstrated favorable drug release behavior under near-infrared laser irradiation, further confirming their potential in combined chemotherapy and phototherapy. *In vitro* cell experiments revealed that the nanoparticles had a high cellular uptake rate, consistent with studies on HA-coated nanoparticles, further validating the effectiveness of HA as a targeting moiety. The *in vitro* experiments showed that P/I NPs significantly inhibited the viability of 4T1 cells and induced apoptosis, similar to the effects of HA-coated nanoparticles in breast cancer treatment. *In vivo* experiments also demonstrated that P/I NPs effectively inhibited tumor growth

with an inhibition rate comparable to other targeted nanoparticle carriers. Fluorescence imaging confirmed the targeted accumulation of P/I NPs at the tumor site, further highlighting the potential of HA–ANI NPs in enhancing therapeutic efficacy. Moreover, no significant damage was observed in the major organs of treated mice, as confirmed by hematoxylin and eosin (H&E) staining, indicating the good biocompatibility and safety of the nanoparticle delivery system. Pathological analysis of the tumor tissues also supported the notion that HA-coated nanoparticles can effectively inhibit tumor growth without affecting normal tissues. In summary, this study not only further expanded the research on targeted drug delivery using HA and the EPR effect but also provided strong theoretical support for the combined use of chemotherapy and phototherapy in treating triple-negative breast cancer. The results suggest that the HA–ANI nanoparticle system has the potential to become an effective strategy for treating various types of cancer.
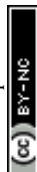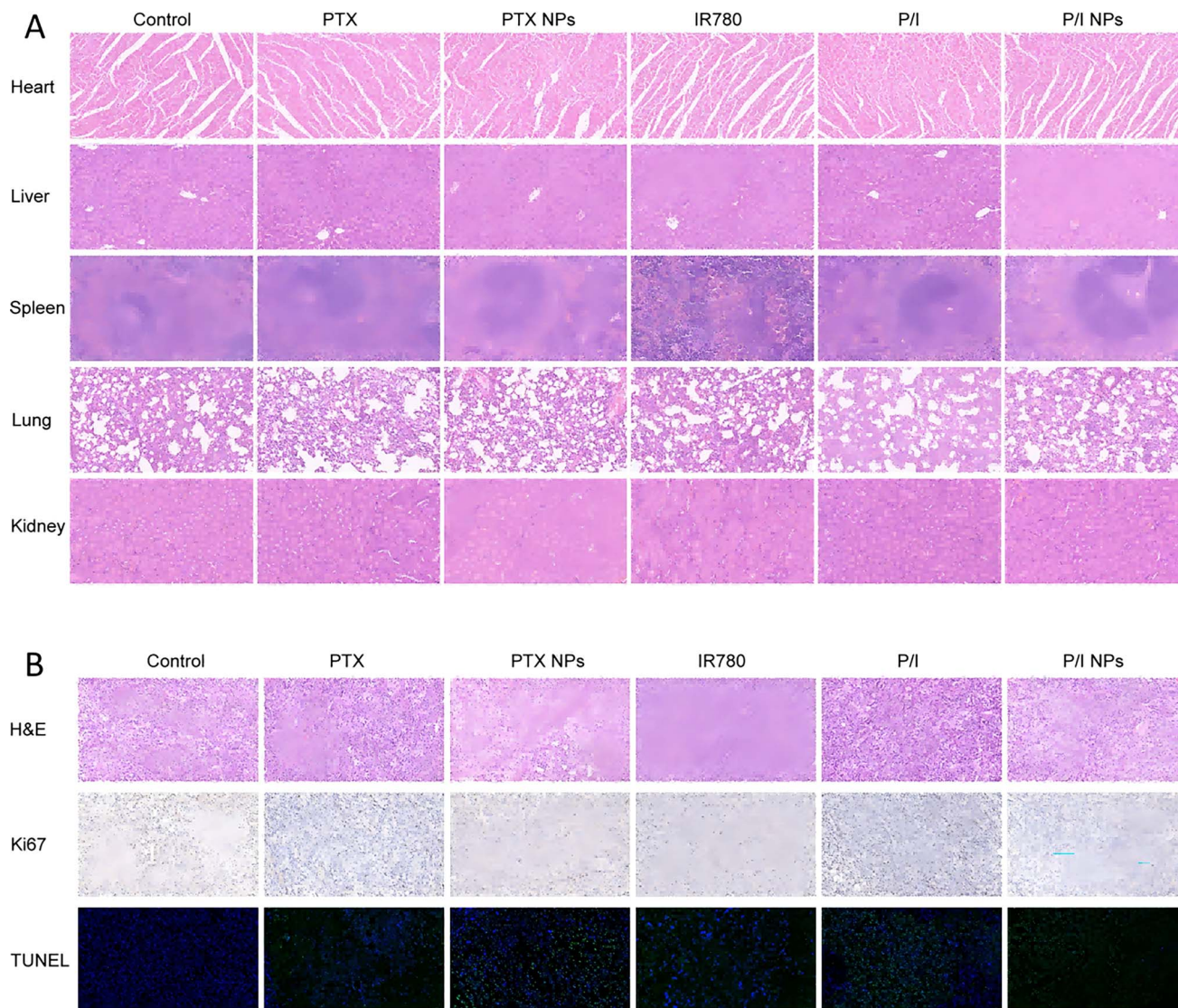
Fig. 14 H&E, TUNEL and Ki67 staining analysis of tumour tissues and the important organs of heart, liver, spleen, lungs and kidneys of mice dissected 13 days after treatment with different groups of drugs. (A) H&E staining results of heart, liver, spleen, lungs and kidneys after treatment; (B) H&E, TUNEL and Ki67 staining results of tumour tissues after treatment. Scale bar: 50 μm.

5 Conclusions

In this study, a nanoparticle with uniform size and good stability was prepared. The release of the nanoparticles was accelerated in a high NADPH tumour environment, and the nanoparticles could be effectively absorbed by 4T1 cells, and had a strong inhibitory effect on cell growth and migration, and promoted cell apoptosis. Animal experiments further demonstrated the inhibitory effect of the nanoparticles on tumours and that they could be targeted to the tumour site without obvious side effects.

Ethical statement

Certificate of laboratory animal welfare ethical review was approved by Hunan Normal University Biomedical Research Animal Welfare Ethics Committee, Approval Number: D202342.

Data availability

The data supporting the findings of this study were collected during the completion of a doctoral dissertation and are currently stored on a personal computer. Due to data protection, they are not available in a public repository. However, the data may be accessed upon reasonable request. Contact Xiaojun Tao *via* email to taoxiaojun1981@outlook.com.

Author contributions

Conceptualization: F. Y., H. L. and Q. L.; methodology: F. Y., H. L. and H. D.; writing—original draft preparation: F. Y., H. L., H. D., R. Z. and Y. Y.; writing—review and editing: H. L. and Q. L.; visualization: H. D., R. Z., Q. L. and H. Y.; project administration: X. T. and H. W.; funding acquisition, H. W. and

H. Y. All authors have reviewed and approved the final version of the manuscript.

Conflicts of interest

There are no conflicts to declare.

Acknowledgements

References

1 X. Zhang, *Arch. Pathol. Lab. Med.*, 2023, **147**, 46–51.

2 K. Asleh, N. Riaz and T. O. Nielsen, *J. Exp. Clin. Cancer Res.*, 2022, **41**, 265.

3 S. Zhu, Y. Wu, B. Song, M. Yi, Y. Yan, Q. Mei and K. Yi, *J. Hematol. Oncol.*, 2023, **16**, 100.

4 G. Bianchini, C. De Angelis, L. Licata and L. Gianni, *Nat. Rev. Clin. Oncol.*, 2022, **19**, 91–113.

5 L. Sun, P. Zhao, M. Chen, J. Leng, Y. Luan, B. Du, J. Yang, Y. Yang and R. Rong, *J. Controlled Release*, 2022, **348**, 672–691.

6 X. Hou, Q. Chen, Y. Fang, L. Zhang, S. Huang, M. Xu, Y. Ren, Z. Shi, Y. Wei and L. Li, *Int. J. Nanomed.*, 2024, 8237–8251.

7 V. M. Dan, R. S. Raveendran and S. Baby, *Mini-Rev. Med. Chem.*, 2021, **21**, 1237–1268.

8 X. Niu, T. Wu, Q. Yin, X. Gu, G. Li, C. Zhou, M. Ma, L. Su, S. Tang, Y. Tian, M. Yang and H. Cui, *Cells*, 2022, **11**, 3094.

9 L. Lei, W. Dai, J. Man, H. Hu, Q. Jin, B. Zhang and Z. Tang, *J. Nanobiotechnol.*, 2023, **21**, 482.

10 M. G. C. Machado, M. A. de Oliveira, E. G. Lanna, R. P. Siqueira, G. Pound-Lana, R. T. Branquinho and V. C. F. Mosqueira, *Biomed. Pharmacother.*, 2022, **145**, 112464.

11 M. Potara, T. Nagy-Simon, M. Focsan, E. Licarete, O. Soritau, A. Vulpoi and S. Astilean, *Colloids Surf., B*, 2021, **203**, 111755.

12 X. Chen, D. Wu and Z. Chen, *MedComm*, 2024, **5**, e643.

13 T. Hu, Y. Huang, J. Liu, C. Shen, F. Wu and Z. He, *Pharmaceutics*, 2023, **15**, 1821.

14 S. Elmehrath, H. L. Nguyen, S. M. Karam, A. Amin and Y. E. Greish, *Nanomaterials*, 2023, **13**, 953.

15 R. Solanki, *et al.*, *J. Drug Delivery Sci. Technol.*, 2022, **77**, 103832.

16 M. Saeedi, O. Vahidi, M. R. Moghbeli, S. Ahmadi, M. Asadnia, O. Akhavan, F. Seidi, M. Rabiee, M. R. Saeb, T. J. Webster, R. S. Varma, E. Sharifi, A. Zarrabi and N. Rabiee, *J. Controlled Release*, 2022, **350**, 175–192.

17 T. Hu, Y. Huang, J. Liu, C. Shen, F. Wu and Z. He, *Pharmaceutics*, 2023, **15**, 1821.

18 J. A. Lebrón, P. López-Cornejo and F. J. Ostos, *Pharmaceutics*, 2022, **14**, 471.

19 J. Fang, *J. Pers. Med.*, 2022, **12**, 95.

20 H. Ding, P. Tan, S. Fu, X. Tian, H. Zhang, X. Ma, Z. Gu and K. Luo, *J. Controlled Release*, 2022, **348**, 206–238.

21 C. Wang, X. Yang, H. Qiu, K. Huang, Q. Xu, B. Zhou, L. Zhang, M. Zhou and X. Yi, *Front. Bioeng. Biotechnol.*, 2023, **11**, 1168192.

22 Z. Deng and S. Liu, *J. Controlled Release*, 2020, **326**, 276–296.

23 W. Hou, R. Liu, S. Bi, Q. He, H. Wang and J. Gu, *Molecules*, 2020, **25**, 5147.

24 M.-H. Qu, R.-F. Zeng, S. Fang, Q.-S. Dai, H.-P. Li and J.-T. Long, *Int. J. Pharm.*, 2014, **474**, 112–122.

25 N. Kharouf, T. W. Flanagan, S.-Y. Hassan, H. Shalaby, M. Khabaz, S.-L. Hassan, M. Megahed, Y. Haikel, S. Santourlidis and M. Hassan, *Cancers*, 2023, **15**, 3147.

26 E. Giusto, L. Žárská, D. F. Beirne, A. Rossi, G. Bassi, A. Ruffini, M. Montesi, D. Montagner, V. Ranc and S. Panseri, *Nanomaterials*, 2022, **12**, 2372.

27 G. Li, J. Zhang, S. Zhang, L. Teng and F. Sun, *J. Controlled Release*, 2023, **362**, 309–324.

28 S. Amorim, C. A. Reis, R. L. Reis and R. A. Pires, *Trends Biotechnol.*, 2021, **39**, 90–104.

29 C. Dong, Y. Wang, W. Zhu, Y. Ma, J. Kim, L. Wei, G. X. Gonzalez and B.-Z. Wang, *ACS Appl. Mater. Interfaces*, 2022, **14**, 6331–6342.

30 C. Buckley, T. R. Montgomery, T. Szank, B. A. Murray, C. Quigley and I. Major, *Int. J. Biol. Macromol.*, 2023, **240**, 124459.

31 V. R. Placencio-Hickok, M. Lauzon, N. Moshayedi, M. Guan, S. Kim, N. Nissen, S. Lo, S. Pandol, B. K. Larson, J. Gong, A. E. Hendifar and A. Osipov, *Pancreatology*, 2022, **22**, 92–97.

32 J. Gong, M. Guan, H. Kim, N. Moshayedi, S. Mehta, G. Cook-Wiens, B. K. Larson, J. Zhou, R. Patel, I. Lapite, V. R. Placencio-Hickok, R. Tuli, R. B. Natale and A. E. Hendifar, *Oncotarget*, 2022, **13**, 1202–1214.

33 G.-e.-S. Chaudhry, A. Akim, M. N. Zafar, N. Safdar, Y.-Y. Sung and T. S. T. Muhammad, *Adv. Pharm. Bull.*, 2021, **11**, 426–438.

34 S. Zhou, J. Xu, Y. Dai, Y. Wei, L. Chen, W. Feng, Y. Chen and X. Ni, *Biomater. Res.*, 2022, **26**, 66.